A Measurement-Based Model of the Electromagnetic Emissions From a Power Inverter

Natalia Bondarenko, Li Zhai, Bingjie Xu, Guanghua Li, Tamar Makharashvili, David Loken, Phil Berger,
Thomas P. Van Doren, *Fellow, IEEE*, and Daryl G. Beetner, *Senior Member, IEEE*

***Abstract*—Rapidly switching semiconductors in modern high power inverter/motor-drive systems generate fast changing voltages and currents which may result in unwanted emissions. While models of power inverters have been built in the past to predict emissions, they are typically "black box" models where the cause of and solution to emissions problems is difficult to analyze. To improve inverter system design strategies, a detailed measurement-based SPICE model of a power inverter system was built in which there is a straightforward correlation between system geometry and parasitic circuit elements. This model was validated through measurements. The model was able to predict transfer characteristics between ports of the inverter within 4 dB from 100 kHz to 100 MHz. Once built, this model was used to identify structures responsible for resonances and to determine possible improvements of the power inverter design to reduce emissions. Measurements of S21 and radiated emissions after adding these improvements demonstrated that they were able to reduce emissions by 10–20 dB, thus confirming the accuracy of the model and its ability to improve understanding of emission mechanisms and to guide development of emissions reduction strategies.**

***Index Terms*—Electromagnetic interference (EMI), electromagnetic modeling, electromagnetic radiation, parameter estimation, variable speed drives.**

I. Introduction

ELECTROMAGNETIC interference (EMI) is a major challenge to design of modern high power inverter/motor drive systems. EMI is mainly generated through fast switching of inverter outputs. Large d*v*/d*t* and d*i*/d*t* components in the output interact with inverter parasitics to create conducted and/or radiated emissions [1]–[3]. The switching times of the insulated-gate bipolar transistors (IGBTs) in power inverters must be fast for efficiency and thermal reasons, so the high values of d*v*/d*t* and d*i*/d*t* cannot be easily reduced. The design of the inverter electronics, heatsink, harness and grounding structure, however, can be modified and filtering can be added to reduce electromagnetic emissions. Ideally, the impact of such mitigation techniques could be evaluated early in the design process through accurate models of the system.

While full-wave models are accurate, applying full-wave models to complex systems like a power inverter is difficult, as they require substantial computational time and memory [4], [5]. More importantly, such full-wave models are often a "black box" that does not directly show which parts of the system are responsible for a particular EMI problem or how to solve the problem without additional simulations and effort. Models of inverters also often require nonlinear elements that cannot be modeled easily with a full-wave solver and should be considered using circuit analysis. An equivalent SPICE-based model which includes the system parasitics is a better approach, since it can give a straightforward correlation between system geometry and parasitic circuit elements and the resulting common-mode (CM) currents.

A SPICE-based model can be obtained from schematics, harness information, and system layout (e.g., the IGBT, heatsink, and enclosure geometry). Several methods are available for extracting parasitic SPICE parameters from a complex geometry [6]–[8]. Many of these methods are based on 3-D finite-element analysis [4], [5] or the partial element equivalent circuit (PEEC) method [9]–[12]. The output from finite-element analysis is not typically a simple SPICE circuit but a black box measure of circuit characteristics, for example, the S parameter values between two ports. The PEEC approach provides a SPICE model of parasitics in terms of RLGC matrices, but may require hundreds or thousands of elements to represent even a simple geometry, which is too many for an intuitive understanding of how the circuit works. Model-order reduction (MOR) techniques may help provide an equivalent circuit representation [13], but these circuits are purely functional and, like the S parameters, do not provide significant physical insight into the inner workings of the device. In [14], equivalent SPICE circuit elements are determined from *Z*-parameters found from 3-D full-wave models. While the resulting circuit is useful, modeling the complete power inverter (whose precise geometry may be unknown) requires substantial time and effort.

Parasitics may also be obtained through measurements or a combination of measurements and full-wave simulations. One approach is to use time-domain reflectometry (TDR) and transmission line theory to extract parasitics [15]. This approach is limited by the ability to accurately extract parasitics which may be much larger or smaller than 50 Ω. Impedance measurements were similarly used in [16] to determine equivalent circuits for some inverter modules. In another recent

---

Manuscript received April 14, 2014; accepted December 2, 2014. Date of publication December 18, 2014; date of current version May 22, 2015. This work was supported in part by the National Science Foundation under Grant 0855878. Recommended for publication by Associate Editor R. Redl.

N. Bondarenko, G. Li, T. Makharashvili, P. Berger, T. P. Van Doren, and D. G. Beetner are with the EMC Laboratory, Missouri University of Science and Technology, Rolla, MO 65409 USA (e-mail: nbcnc@mst.edu; glbm4@mst.edu; tm2p8@mst.edu; bergerphi@mst.edu; vandoren@mst.edu; daryl@mst.edu).

L. Zhai is with the Beijing Institute of Technology, Beijing 100081, China (e-mail: Zhaili26@bit.edu.cn).

B. Xu is with the Huazhong University of Science & Technology, Wuhan 430074, China (e-mail: bingjiexu.molly@gmail.com).

D. Loken is with John Deere Electronic Solutions, Fargo, ND 58102 USA (e-mail: lokendavidm@johndeere.com).

Color versions of one or more of the figures in this paper are available online at http://ieeexplore.ieee.org.

Digital Object Identifier 10.1109/TPEL.2014.2384030

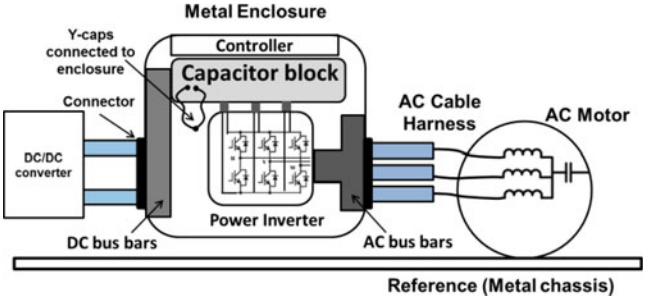

Fig. 1. Power inverter/motor system.

study [17], a measurement-based inverter model was presented, where scattering parameters were converted to equivalent CM and differential-mode (DM) impedances. Although the model is based on measurement, it is still a "black box" model of the inverter which does not represent specific parasitics. A study is presented in [18] which develops a low-frequency parameter-based model of induction machines using DM and CM impedance measurements. A number of other studies [4], [19], [20] have demonstrated the usefulness of using a combination of measurements and simulations.

Existing studies lack the development of a simple model for a complete power inverter system and do not demonstrate how to use this model to reduce radiated emissions. A methodology is presented in the following paper to build a rather simple, yet accurate, equivalent model of a real power inverter which has a clear correlation between parasitic circuit elements and system geometry. The method is applicable up to 100 MHz, which is above the frequency where problems are typically seen in power inverter systems, and was the maximum frequency of interest specified by our industry partners. For this application, the power inverter and attached motor (see Fig. 1) were divided into subsystems representing the dc cables, dc-link capacitance block with dc-bus bars, IGBT module, ac-bus bars, ac cables, and motor/load. A simple equivalent model was built for each subsystem and validated through measurements. The subsystem models were assembled to create a model of the complete system. This relatively simple model was used to find the system components responsible for the most important resonances and then, based on the understanding of these resonances, to demonstrate how changes could be made to the system to mitigate these resonances. The effectiveness of the mitigation strategies was demonstrated through measurements of the output voltage and radiated emissions.

II. CONSTRUCTION OF THE EQUIVALENT CIRCUIT

An example of the power inverter/motor system is shown in Fig. 1. The equivalent circuit should include information about the cables (both dc and ac), parasitic inductances of the Y capacitors, parasitic inductances due to the dc-link capacitor, inductances due to the terminals of the IGBT module, the capacitances between the IGBT and chassis, and the high-frequency impedance of the motor (or dummy load). As the pulse width modulated inverter structure is symmetrical, it is only necessary to model the behavior of one inverter leg.

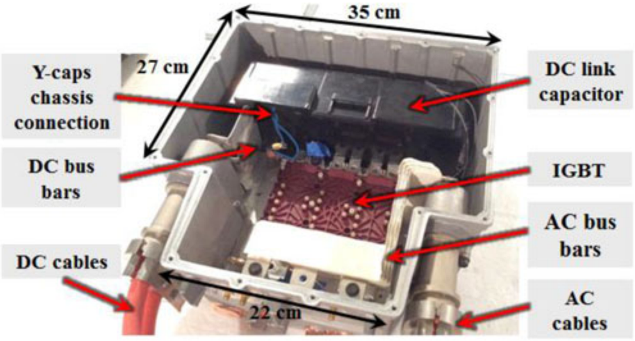

Fig. 2. Power inverter enclosure with dc-link capacitor, dc-bus bars, IGBT, and ac-bus bars.

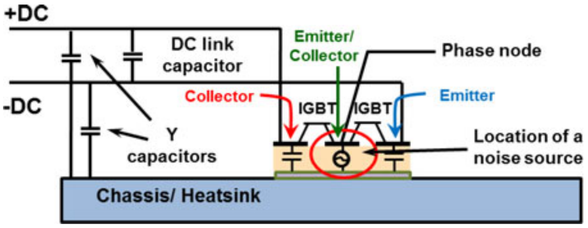

Fig. 3. Location of the main "noise" source inside the IGBT module.

The inverter under study is housed in a metal enclosure (see Fig. 2) and generally well shielded from its environment. All power cables going in or out of the enclosure are shielded, with the shields making a good 360° connection at the enclosure. The one location where there is a good potential to drive parasitic antennas and cause radiated emissions is at the connection between the ac cables and the motor. While a good 360° connection of the shield at this location may be used, in many cases a long pigtail is used to connect the shield to the motor housing. Even with a good connection, the RF shielding within the motor itself is highly variable. Because the cable connection to the motor is the only place where emissions may reasonably be generated by this well-shielded device, the voltage between the inner conductor and shield of the ac cable at the connection to the motor was used as a reference when proposing schemes to mitigate emissions. Later measurements confirm the suitability of this approach.

A simple model of the IGBT is illustrated in Fig. 3. For each IGBT phase leg, there are parasitic capacitances from the emitter to chassis, from collector to chassis, and from phase (the emitter/collector node) to chassis. Most emissions are expected to result from the voltage between the phase node and chassis, since the switching occurs at this node and this CM voltage can directly drive a voltage between the center conductor and shield of the ac cable at the motor connection.

The parasitic antenna that drives emissions is primarily composed of the shields of the cables and the motor and inverter housings. The characteristics of this antenna cannot be changed significantly during testing, since standards specify the placement of these components. Since this antenna is driven primarily by the voltage at the end of the ac cable, and this voltage results primarily from the voltage between the IGBT phase node

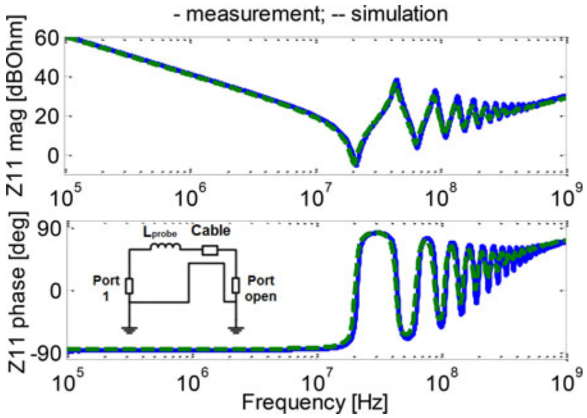

Fig. 4. Validation of the transmission line model for the open-ended dc cable. Measured values are shown with a solid line and simulated values with a dashed line.

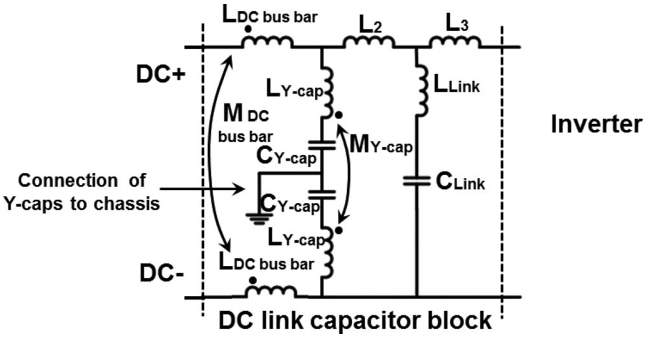

Fig. 5. Schematic of dc link.

and chassis, the value of S21 between the phase-node-to-chassis voltage and the center-conductor-to-shield voltage of the ac cable connection to the motor is critical to understanding and mitigating emissions mechanisms.

A. AC and DC Cables

The dc and ac cables were modeled as transmission lines. This model requires information like the characteristic impedance, dielectric constant of the insulation, and loss tangent. The datasheet provided only geometrical information, so measurements were made with a TDR and a vector network analyzer and parameters were determined from the measurements. Fig. 4 shows a comparison of the predicted and measured impedance, where simulations were performed using a transmission line model of a 1.86 m long cable with $Z_0 = 8.56\,\Omega$, $\varepsilon_r = 2.65$, and loss tangent of 0.108. A 4 nH parasitic inductance was placed in series with the cable to model the SMA connector used to make the measurement.

The dc-link capacitor block consists of a dc-link capacitance (with nominal $C = 1028\ \mu$F) and two Y-capacitances (with nominal $C = 0.98\ \mu$F), as illustrated in the model shown in Fig. 5. This circuit template was constructed with some information of circuit geometry. Parameter values could then be filled in later through measurements. While inductance is a property of loops, an approximate model was constructed using partial inductances. The inductances $L_{\text{DC-bus bar}}$ and $M_{\text{DC-bus bar}}$ are due to the bus bars of the capacitor block, L2 and L_{Link} are parasitic inductances associated with the link capacitor, $L_{\text{y-cap}}$ and $M_{\text{y-cap}}$ are associated with the Y-capacitors, and L3 is the inductance due to the output of the capacitor block (where it connects to the IGBT module). The simple model without mutual inductances was used initially, but later it was found useful to split $L_{\text{DC-bus bar}}$ between the dc+ and dc– buses, and to include the mutual inductance between the buses. The mutual inductances help to differentiate between the impedance seen by CM and DM currents.

TABLE I
EQUATIONS DESCRIBING DC-LINK CAPACITOR BLOCK INDUCTANCES

Measurement	Equation
DC cable, dc-link block, Y-caps	$L_{@1\,\text{MHz}} \approx L_{\text{DCcable}} + L_{\text{DC}-\text{busbar}} + \frac{L_{Y-\text{cap}} + M_{Y-\text{cap}}}{2}$
DC cable, dc-link block,	$L_{@2\,\text{MHz}} \approx L_{\text{DCcable}} + L_{\text{DCbusbar}} + L_2 + L_{\text{Link}}$
DC link, looking into Y-caps	$L_{@10\,\text{MHz}} \approx 2(L_{Y-\text{cap}} - M_{Y-\text{cap}}) + L_2 + L_{\text{Link}}$
DC-link input shorted, Y-caps open	$L_{@14\,\text{MHz}} \approx L_3 + L_{\text{Link}} \| (L_{\text{DC}-\text{busbar}} + L_2)$
DC link, Y-caps open	$L_{@11\,\text{MHz}} \approx L_3 + L_{\text{Link}}$

B. DC Link

Measurements of the dc-link capacitor block were performed with the capacitor block alone and also with the block connected to the dc cable to determine the values of the parasitic inductances due to Y-capacitors and dc-bus bars. A number of Z11 and Z22 measurements were performed while other ports were made open or short. The value of Z11 looking into the Y-capacitors was also obtained by measuring impedance between one of the Y-capacitor connections and the chassis. The values of the parasitic inductances could not be determined from a single measurement, but could be determined mathematically from the set of measurements. The measurements and associated equations are illustrated in Table I, where parameters used in the equations are given in Fig. 5.

Example measurements are demonstrated in Fig. 6. In the measurement in Fig. 6(a), Port 1 is at the beginning of the dc+ cable and Port 2 is at the output of the dc capacitor block. The dc– cable is not connected. The Y-capacitors are connected to the chassis. The shields of both dc cables are connected to the enclosure. At about 1 MHz, the capacitance due to the dc block ($C_{\text{Link}} = 1028\ \mu$F) looks like a short, the current returns to the chassis through both Y-capacitors, and the input impedance is equivalent to a 272 nH inductor. Tracing the currents during the Z11 measurement at this frequency gives

$$L_{1\,\text{MHz}} \approx L_{\text{DC+cable}} + L_{\text{DC}-\text{bus bar}} + \frac{L_{Y-\text{cap}} + M_{Y-\text{cap}}}{2} \approx 272\,\text{nH}. \quad (1)$$

An additional measurement of the $L_{Y-\text{cap}}$ inductance is made by breaking the connection of one Y-capacitor to the chassis, and measuring the impedance looking into the Y-capacitor break, as shown in Fig. 6(b). Tracing this impedance at10 MHz

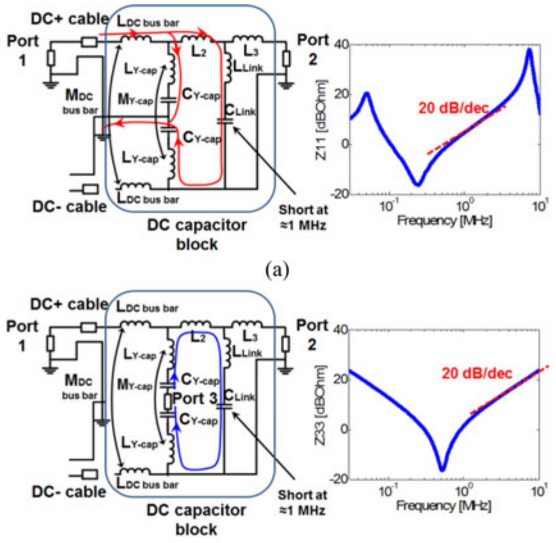

(a)

(b)

Fig. 6. Example measurement made to obtain the dc-link capacitor block parasitics (a) from connected dc+ cable, dc link and Y-caps connected to chassis, at 1 MHz and (b) from impedance looking into Y-caps at 10 MHz.

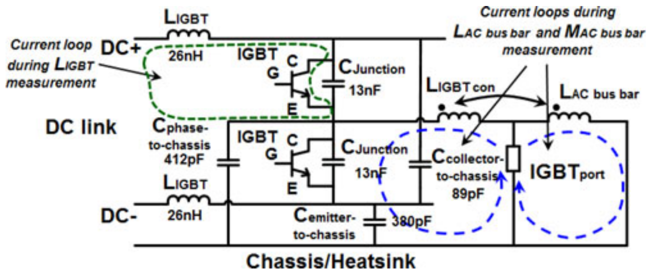

Fig. 7. Equivalent model of one phase of the IGBT module, IGBT connection, and ac-bus bar.

gives

$$L_{10\,\mathrm{MHz}} \approx 2\left(L_{Y-\mathrm{cap}} + M_{Y-\mathrm{cap}}\right) + L_2 + L_{\mathrm{Link}} \approx 214\,\mathrm{nH}. \tag{2}$$

Using these equations (along with other measurements), the mutual inductance $M_{Y-\mathrm{cap}}$ was found to be 108 nH, and the self-inductance associated with each Y-capacitor to be about 150 nH. As demonstrated by the relative size of $M_{Y-\mathrm{cap}}$ and $L_{Y-\mathrm{cap}}$, the mutual inductance could not be ignored. The importance of mutual inductances between busses was noted on several occasions while developing the model.

C. IGBT

To model the IGBT module, two Z11 measurements were made looking into the output of the module while the input was open or short. These measurements were used to determine the IGBT junction capacitance and the loop inductance due to the IGBT bus bars (provided this inductance is not dominated by the inductance of the probe used to make the measurement). The measured junction capacitance across both the pull-up and pull-down IGBTs when the dc– and dc+ terminals were shorted was about 13 nF, as illustrated in Fig. 7. The IGBT bus bar inductance was determined from a Z11 measurement looking into the IGBT when a return was provided using a large metal plate. This measurement gives an estimate of the loop inductance associated with one phase leg of the IGBT module. This inductance was found to be approximately 26 nH. The measured parasitic capacitance from the phase node to chassis (across the direct bonded copper substrate) was measured using an *LCR* meter. The measured value was about 850 pF. This capacitance is a distributed capacitance (from collector to chassis, from emitter to chassis, and from the phased node to chassis) as shown in Fig. 3. From the size of the plates collector, emitter, and phase nodes plates in the IGBT, and the measured total capacitance, the size of each parasitic capacitances was estimated to be 412, 380, and 89 pF, as shown in Fig. 7 [16]. As will be demonstrated later, it is the total value of capacitance, 850 pF, which is critical to resonances in the circuit.

D. AC-Bus Bars

To estimate the loop inductance associated with the ac-bus bars, which carry current from the output of the IGBT to the ac cables (see Fig. 2), a measurement of Z11 looking into the output of the IGBT module was made while its input was open and the end of ac-bus bars was shorted to the enclosure. This setup creates two current loops: one from the input port through the ac-bus bars and chassis and another loop from the input port through the IGBT connection, through the parasitic capacitance to the chassis as indicated in Fig. 7. These currents must return to Port 1 through a metal connector approximately 2 cm long (connecting the SMA connector to the chassis). The shared return path through the connector creates a large mutual inductance between the loop associate with the ac-bus bar and the loop associated with the IGBT connection. The partial self-inductances were directly extracted from Z11 and are about 130 and 25 nH, respectively. The mutual term was approximated from a measurement of S21 for a port between the phase node to chassis and a port at the end of the ac cable. As the length of the metal connector is about 2 cm, the mutual inductance should be around 10–20 nH. The mutual inductance was found to be about 12 nH by comparing the simulated and measured values of S21 while tuning the mutual inductance.

E. Complete System

The model of the complete circuit was assembled from the models of the individual subsystems, as shown in Fig. 8. This model is for a single phase leg of the IGBT and a single ac cable. The motor is not shown, since measurements determined its impedance were too large to be significant over the frequency band of interest. The values of the circuit parameters are shown in Table II.

III. VALIDATION OF THE COMPLETE MODEL

Each subsystem was modeled and characterized separately because accurate models of these systems cannot reasonably be obtained using only measurements of the complete system. Characterizing the subsystems separately, however, assumes that the parasitic coupling between subsystems is small. This

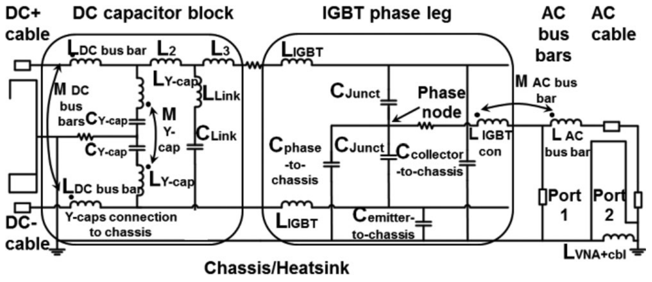

Fig. 8. Complete equivalent circuit model. Port one: between phase node and chassis. Port 2: between inner and outer conductors at the end of the ac cable.

TABLE II
VALUES OF COMPONENTS WITHIN EQUIVALENT CIRCUIT

Component	Value	Component	Value
$L_{\mathrm{DC-bus\,bar}}$	50 nH	$M_{\mathrm{DC-bus\,bar}}$	40 nH
$C_{Y-\mathrm{cap}}$	700 nF	$L_{Y-\mathrm{cap}}$	150 nH
$M_{Y-\mathrm{cap}}$	108 nH	L_2	2 nH
L_3	12 nH	C_{Link}	1028 μF
L_{Link}	10 nH	C_{Junction}	13 nF
L_{IGBT}	26 nH	$C_{\mathrm{phase-to-chassis}}$	412 pF
$C_{\mathrm{collector-to-chassis}}$	89 pF	$C_{\mathrm{emitter-to-chassis}}$	380 pF
$L_{\mathrm{IGBT\ con}}$	25 nH	$L_{\mathrm{AC-bus\,bar}}$	130 nH
$M_{\mathrm{AC-bus\,bar}}$	12 nH		

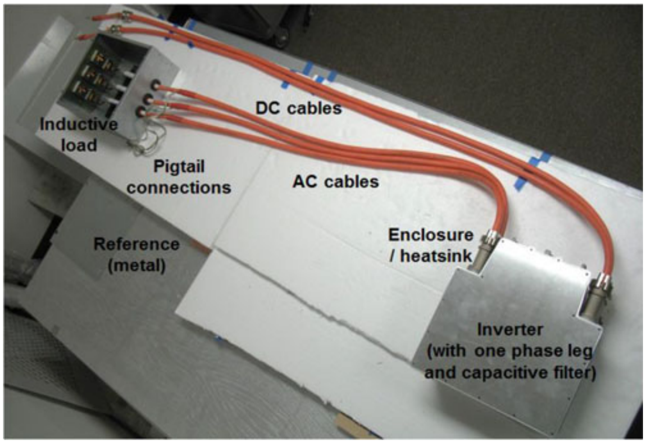

Fig. 9. Measurement setup used to validate overall inverter model.

assumption is reasonable because of the distances between components, but must be verified through measurements of the complete, assembled system.

The model was validated, in part, by comparing the input impedance and/or S-parameters at ports of both the individual subsystems as well as the overall model. The complete circuit model was validated using the experimental setup shown in Fig. 9. Port 1 was placed between the phase node and chassis (at the source of switching) and Port 2 was placed between the inner and outer conductors at the end of the ac cable (where the noise is most likely to drive radiated emissions). Comparisons of the simulated and measured transfer characteristics between these ports are shown in Fig. 10 from 100 kHz to 1 GHz. Measured and simulated values of Z11 and Z22 are presented in Fig. 11.

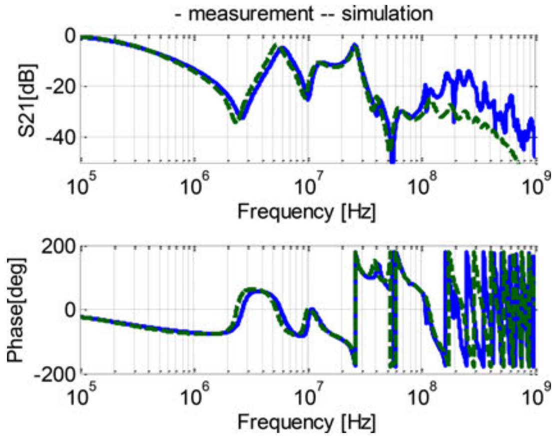

Fig. 10. Magnitude and phase of S21 between the phase node and the output of the ac cable.

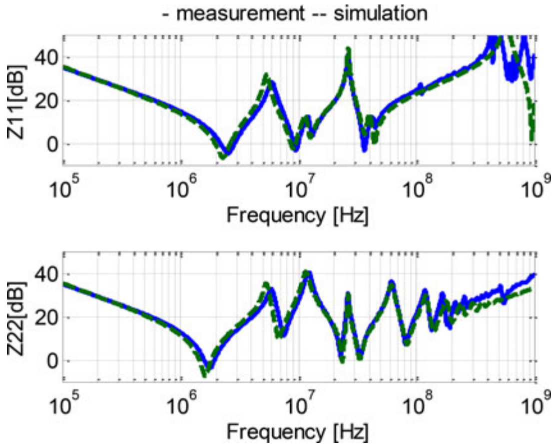

Fig. 11. Magnitude of Z11 looking into the phase node and Z22 looking into the ac cable output.

The model describes behavior of the system at these ports within 4 dB from 100 kHz to 100 MHz. It should be noted that there is some difference in the level of S21 for frequencies higher than 100 MHz, which may be caused by parasitic couplings between the subsystems, which were not included in the model, but that become important at those frequencies.

IV. CORRELATION OF SYSTEM RESONANCES WITH GEOMETRY

A significant advantage of a simple model is that one can more easily understand the causes of specific behaviors and how to modify the system to improve this behavior. Resonances within the inverter cause peaks in the transfer characteristics from the phase node to the output of the ac cable, which may also cause peaks in the radiated emissions. If one can understand which components or current paths are involved in these resonances, one can better understand how to remove or mitigate their effect.

The most critical resonant frequencies associated with this power inverter system are around 5, 10, and 30 MHz, as seen in the values of S21 in Fig. 10 and later in measurements of radiated emissions (see Fig. 18). When Port 1 is between the phase node and chassis, Z11 and S21 are closely related

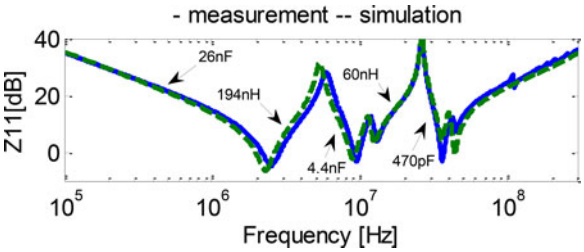

Fig. 12. Magnitude of Z11 and corresponding value of parasitics.

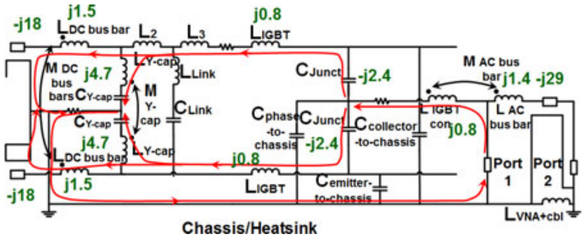

Fig. 13. Analysis of current path for one problematic frequency (5 MHz).

since both are highly dependent on the impedance looking into the IGBT. Since Z11 is easier to relate to inductance or capacitance, Z11 was studied to identify causes of resonances. Fig. 12 is marked with a value of inductance or capacitance that *might* be associated with each portion of the curve. These approximations were used to help guide the analysis.

To illustrate the methodology used to determine the current path and elements responsible for each resonance, consider the resonance at 5 MHz. To help find the elements responsible for the resonance, the impedance of each circuit element at 5 MHz was determined as shown in Fig. 13. At 5 MHz, the impedance of the dc cable is about $-j18\ \Omega$:

$$Z_{\text{DCcable}} = \frac{1}{j\omega C_{\text{cable}}} = \frac{1}{j2\pi f^{*} c_{\text{pul}}{}^{*} l_{\text{cable}}} \approx -j18\,\Omega \qquad (3)$$

where c_{pul} is the capacitance per-unit-length of the cable and l_{cable} is its length. The effective impedance of the two dc cables in parallel is about $-j9\ \Omega$. If the inductance due to dc-bus bars $(j2\pi f(L+M) \approx j3\,\Omega)$ is included, the effective impedance for the dc cable and bus bars is about $-j6\ \Omega$. At 5 MHz, the effective impedance associated with the two *Y*-capacitors in parallel is about $j6\ \Omega$:

$$Z_{Y-\text{caps}+} = j\omega\left(\frac{L_{y-\text{caps}}}{2} + M_{Y-\text{caps}}\right) \approx j6\,\Omega. \qquad (4)$$

While other impedances may also play a role, the impedances of the dc cable capacitance and *Y*-cap inductance are sufficiently close to reliably identify these components as responsible for the resonance around 5 MHz.

A similar analysis was conducted at other resonant frequencies. The elements determined to be responsible for critical resonances are listed in Table III.

TABLE III
ELEMENTS RESPONSIBLE FOR RESONANCES

Frequency	Responsible elements
Below 2 MHz	IGBT collector to emitter capacitances (26 nF total)
2 MHz resonance	Collector to emitter capacitances of IGBT and inductance of *Y*-caps
5 MHz resonance	Capacitances of dc cables and inductance of *Y*-caps
9 MHz resonance	Transmission line resonance of dc cables and additional series inductance
10 MHz resonance	Inductance of the dc-bus bars and cable resonating with the capacitance looking toward the ac-bus bar and cables
30 MHz resonance	IGBT capacitance between the dc+, dc–, and phase nodes to the chassis (881 pF) and the effective inductance of the ac + dc cables + bus bars

V. MITIGATION OF SYSTEM RESONANCES

The impact of resonances within the inverter can be reduced by lowering their quality factor, or in some cases by changing the frequency at which they occur (thus moving them to a frequency which is unimportant). Some possibilities for mitigating the impact of resonances at 5, 10, and 30 MHz were proposed and tested.

In general, to reduce the amount of energy coupled from the noise source between the phase node and chassis to the end of the ac cables, the overall magnitude of S21 between these ports should be reduced. The equivalent model shows that any significant increase in impedance of the ac cable will reduce S21 and thus should reduce emissions. For example, ferrites around the set of ac cables should decrease S21 since the CM impedance from the phase-node to motor will increase (a ferrite cannot be added to an individual cable because the high intended current would saturate the ferrite). Similarly, any significant decrease in the impedance between the ac cable and shield will reduce emissions. For example, adding a filtered connector (possibly with some losses) to the ac cable should decrease S21. While this suggestion was added for completeness, it should be noted that adding capacitance to any switching node is challenging due to the substantial current this capacitor may consume during operation.

Mitigation strategies depend on which components become important at specific frequencies. For example, at 5 MHz, where the resonance includes CM current through the *Y*-capacitors, a ferrite around the capacitor connections can be used to add loss and reduce the quality factor of the resonance. Similarly at 5 MHz, a lossy capacitive filter (connected with low inductance) could be added in front of the dc cables, with a larger capacitance than the dc cables, so the 5 MHz resonance occurs between the *Y*-capacitor inductance and the lossy capacitive filter, rather than the capacitance of the cables. Placing a lossy capacitor across the dc cables is reasonable since the high-frequency voltage on the dc cables is low. This resonance also involves CM current flowing through the dc-bus bars, which implies that a ferrite choke around the bus bars could also add loss to reduce this resonance.

A similar analysis was performed at other resonant frequencies to determine potential mitigation strategies. These strategies were tested as explained in the following section. Strategies

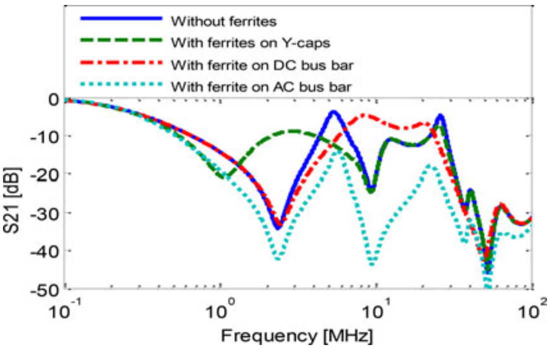

Fig. 14. Change in S21 from added low-frequency ferrites.

included adding ferrite chokes to the *Y*-capacitors, dc-bus bar, ac-bus bar, and adding an *RC* filter to the dc cables and ac-bus bar. A combination of these countermeasures (using a model of a real ferrite choke) was also investigated to demonstrate their overall impact. Individual strategies were tested through simulation. The best of the strategies was validated through measurements.

A. Adding Low Frequency Ferrite Chokes

Low frequency ferrite chokes were added in simulation to the *Y*-capacitors, the dc-bus bars, and the ac-bus bars. The ferrites were modeled as simple parallel *RLC* circuits, with an associated mutual inductance with the circuit sharing the choke. Values of *R*, *L*, and *C* were chosen similar to parameters for commercially available ferrites ($R = 20\ \Omega$, $L = 12\ \mu$H, and $C = 2$ pF). The ferrite choke significantly reduced the peak values of S21 as demonstrated in Fig. 14.

B. Adding RC Filters

An *RC* filter was added to the dc and the ac-bus bars. The capacitance of the filter was set so that the filter would generally have a lower impedance than the dc cable, and thus would impact resonant peaks that would normally be due to the dc cable. In this study, it was found that adding an *RC* filter to the dc cables is more effective at 5 MHz at reducing the resonance peak than adding a low-frequency ferrite choke, especially when the capacitance value is higher than 1 nF. When the capacitance is increased, the peak of S21 is mitigated more effectively. The series resistance of the *RC* filter should be greater than about 2 Ω.

While the ac cables were not initially identified as part of the resonance at 5 MHz, adding the capacitive filter to the ac cables made them more important at lower frequencies, so the filter also had an impact at 5 MHz. In general, the larger the value of capacitance, the greater the reduction in emissions.

C. Combined Mitigation Strategies

The impact of a combination of the proposed mitigation strategies is shown in Fig. 15. The most effective reduction of emissions was obtained when *RC* filters ($C = 50$ nF, $R = 10\ \Omega$) were added between the dc cables and the shield and a low-frequency ferrite choke ($C = 60$ pF, $L = 12\ \mu$H, and $R = 38\ \Omega$) was added to the ac-bus bars. This strategy was able to reduce values of S21 by 10–20 dB at critical resonant frequencies.

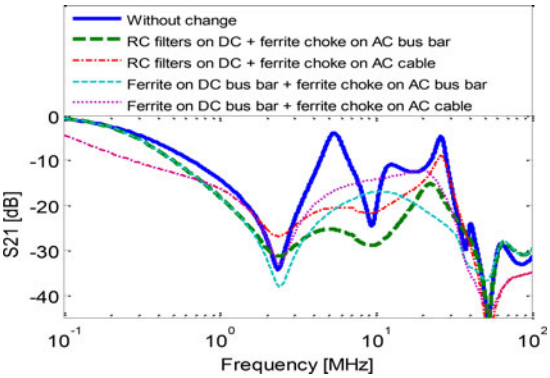

Fig. 15. Predicted effect of combined countermeasures on S21.

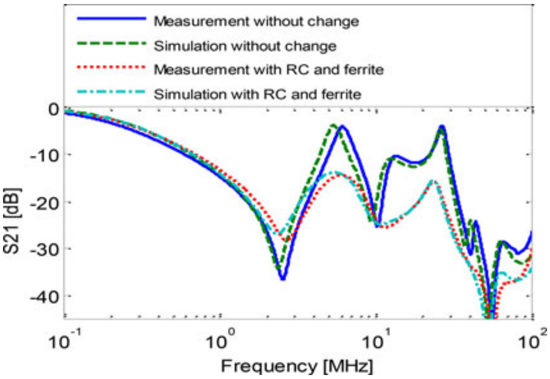

Fig. 16. Measured and simulated values of S21 when *RC* filters and a ferrite are added to the inverter.

D. Validation of the Mitigation Techniques

Two of the mitigation techniques discussed above were applied to the real system. Specifically *RC* filters ($C = 56$ nF, $R = 13\ \Omega$) were added to the dc-bus bars and a ferrite choke (high frequency ferrite by Laird) was added to the ac-bus bar. The ferrite was modeled as a parallel *RLC* circuit (60 Ω, 0.35 μH, 0.1 pF), which was found from datasheet and measurement information. Comparison of measured and predicted values of S21 is shown in Fig. 16. The values match within a few decibels from 100 kHz to 100 MHz. Some disagreement is expected, particularly at high frequencies, because of difficulty in modeling the ferrite.

VI. Radiated Emissions

To further validate the model and demonstrate its effectiveness, changes in radiated emissions were predicted and measured while using the mitigation strategies. Radiated emissions were measured inside a semi anechoic chamber, as shown in Fig. 17. The IGBT phase node was driven with a rectangular pulse to mimic a switching noise source. The measurement setup

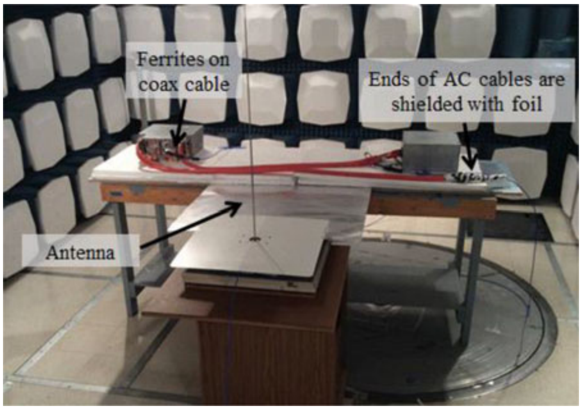

Fig. 17. Setup used for radiated emissions measurements.

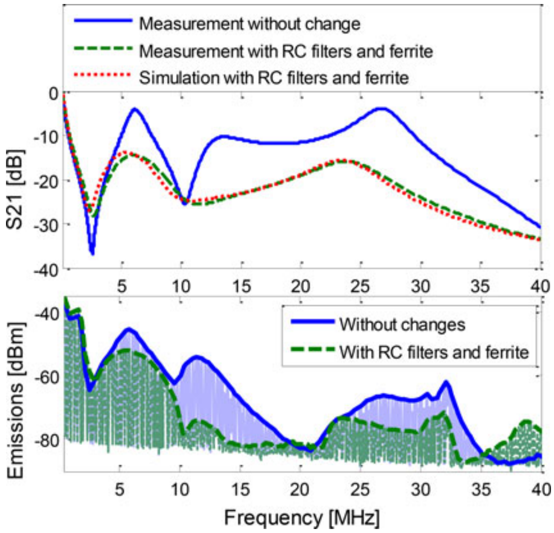

Fig. 18. Correlation between changes in S21 and radiated emissions.

is similar to the CISPR 25 standard. During measurement, the ends of the dc cables were shielded with foil, since in the real setup the shields are connected at 360° to the chamber wall and the ends are thus well shielded. Fig. 18 shows the predicted impact of the mitigation strategies on S21 and the measured impact on radiated emissions. The predicted changes in S21 correlate well with the changes in the radiated emissions up to about 35 MHz. The correlation is not perfect, as adding circuitry can change the interaction between the circuit and the parasitic radiating antenna (for example, changing the antenna resonance). While the model cannot predict such changes, as it does not include a model of the antenna, it still provides good guidance toward the impact of design changes on radiation.

VII. GENERAL METHODOLOGY

While this paper demonstrates the development of a model for a specific power inverter, the methodology can be applied to more general power systems. The model can be developed in the following steps:

Step 1: Divide main system into subsystems for analysis.

Step 2: Estimate rough equivalent model based on parasitics associated with subsystem geometry (e.g., for cables—a transmission line model, for dc link—a combination of link capacitor, Y capacitors, some related bus bar inductances, etc.).

Step 3: Identify the location of the main noise source (for a power inverter usually between the phase node and chassis) and the most critical point where energy could be coupled to cables or other antenna structures (e.g., at the end of the ac cables). These locations are used as ports.

Step 4: Perform network parameters measurements on each subsystem to identify the values of parasitic R, L, and Cs.

Step 5: Assemble complete model from equivalent models of all subsystems. Validate model with measurements and make minor reasonable adjustments as needed. During this step, it may be necessary to adjust for coupling between subsystems that was not accounted for in steps 2–4.

Step 6: Correlate circuit elements (representing real geometry components) of the model with the most important resonances of the system by tracing currents at these resonant frequencies.

Step 7: Use critical circuit elements at (or between) resonances to determine practical countermeasures to mitigate or reduce unwanted emissions.

Critical to this method is dividing the system into simple subcomponents that can be characterized with simple models, and then using the overall (simple) model to understand the root components involved at frequencies where problems occur.

VIII. CONCLUSION

The development and analysis of a model for a complex power system were illustrated in this paper. While the methodology was applied to a power inverter system, it can be applied to other systems as well, where frequencies of interest are below 100 MHz. The equivalent model contains only the most important parasitic elements of the system. Each element can be clearly correlated with real system geometry. The model developed here was able to describe the impedance of a real inverter system well from 100 kHz to 100 MHz. Simulations of S21 for this system showed resonances at frequencies similar to those at which peak radiation has been observed from the real system.

A substantial advantage of a simple circuit representation is that it allows analytic determination of the possible causes of and mitigations strategies for emissions. This process is possible because the circuit is simple and because circuit elements are directly correlated with physical structures within the system. An analysis of the inverter studied here revealed the parasitics responsible for resonances associated with peak emissions. Recommendations to mitigate emissions were made based on the elements and current paths involved in these resonances. The most effective reduction of emissions was found using a combination of an RC filter added between the dc cable and chassis and a low-frequency ferrite choke added on the ac-bus bars, which was validated by measurements.

100 MHz was the highest frequency of interest for the power inverter studied here. Below 100 MHz, there was no significant parasitic coupling between the subsystems, which allowed the subsystems to be characterized separately. At higher

frequencies, parasitic coupling between systems might not be ignored. For example, enclosure resonances may allow efficient coupling between components that are electrically far apart. Parasitic coupling between subsystems may also be an issue at low frequencies for other inverter systems. Parasitic coupling between subsystems was not explored in this paper. This possibility must be checked through validation measurements of the overall system impedances, and accounted for when needed.

While the proposed model does not directly predict the radiated emissions, since it does not include a model of the parasitic radiating antenna, it can still be used to understand and mitigate radiation problems. The validity of this approach was demonstrated by measurement which showed that it was able to effectively predict changes in radiated emissions as a result of adding filtering strategies to the design.

REFERENCES

[1] E. Zhong and T. A. Lipo, "Improvements in EMC performance of inverter-fed motor drives," *IEEE Trans. Ind. Appl.*, vol. 31, no. 6, pp. 1247–1256, Nov./Dec. 1995.

[2] L. Ran, S. Gokani, J. Clare, K. J. Bradley, and C. Christopoulos, "Conducted electromagnetic emissions in induction motor drive systems. Part I: Time domain analysis and identification of dominant modes," *IEEE Trans. Power Electron.*, vol. 13, no. 4, pp. 757–767, Jul. 1998.

[3] G. Skibinski, J. Pankau, R. Sladky, and J. Campbell, "Generation, control and regulation of EMI from AC drives," in *Proc. Conf. Rec. IEEE-IAS Annu. Meeting*, 1997, pp. 1571–1583.

[4] S. Chen, T. W. Nehl, J.-S. Lai, X. Huang, E. Pepa, R. de Doncker, and I. Voss, "Toward EMI prediction of a PM moor drive for automotive applications," in *Proc. IEEE Appl. Power Electron. Conf.*, Miami, FL, USA, 2003, pp. 14–22.

[5] J.-S. Lai, X. Huang, E. Pepa, S. Chen, and T. W. Nehl, "Inverter EMI modeling and simulation methodologies," *IEEE Trans. Ind. Electron.*, vol. 53, no. 3, pp. 736–744, Jun. 2006.

[6] E. Falck, M. Stoisiek, and G. Wachutka, "Modeling of parasitic inductive effects in power modules," in *Proc. IEEE Int. Symp. Power Semicond. Devices IC's*, Weimar, Germany, May 1997, pp. 129–132.

[7] K. Xing, F. C. Lee, and D. Borojevic, "Extraction of parasitics within wire-bond IGBT modules," in *Proc. IEEE Appl. Power Electron. Conf.*, 1998, pp. 497–503.

[8] J. L. Schanen, E. Clavel, and J. Roudet, "Modeling of low inductive busbar connections," *IEEE Ind. Appl. Mag.*, vol. 2, no. 5, pp. 39–43, Sep./Oct. 1996.

[9] V. Ardon, J. Aime, O. Chadebec, E. Clavel, J.-M. Guichon, and E. Vialardi, "EMC modeling of an industrial variable speed drive with an adapted PEEC method," *IEEE Trans. Magn.*, vol. 46, no. 8, pp. 2892–2898, Aug. 2010.

[10] V. Ardon, J. Aime, O. Chadebec, E. Clavel, and E. Vialardi, "MoM and PEEC method to reach a complete equivalent circuit of a static converter," in *Proc. 20th Int. Zurich Symp. Electromagn. Compat.*, Zurich, Switzerland, Jan. 2009, pp. 273–276.

[11] A. Ruehli, "Equivalent circuit models for three-dimensional multiconductor systems," *IEEE Trans. Microw. Theory Tech.*, vol. MTT-22, no. 3, pp. 216–221, Mar. 1974.

[12] M. Lionet, R. Prades, Y. L. Floch, E. Clavel, J. L. Schanen, and J. M. Guichon, "Improving conducted EMI forecasting with accurate layout modeling," presented at theProc. *IEEE Symposium on Embedded EMC*, Rouen, France, 2007.

[13] T. Witting, R. Schuhmann, and T. Weiland, "Model order reduction for large systems in computational electromagnetics," *Linear Algebra Appl.*, vol. 415, nos. 2/3, pp. 499–530, 2006.

[14] F. Traub, J. Hansen, W. Ackermann, and T. Weiland, "Generation of physical equivalent circuit using 3D simulations," in *Proc. IEEE Int. Symp. Electromagn. Compat.*, 2012, pp. 486–491.

[15] H. Zhu, A. R. Hefner, and J. Lai, "Characterization of power electronics system interconnect parasitics using time domain reflectometer," in *Proc. IEEE Power Electron. Spec. Conf.*, Fukuoka, Japan, May 17–22, 1998, vol. 2, pp. 1937–1943.

[16] L. Yang and W. G. H. Odendaal, "Measurement-based characterization method for integrated power electronics modules," *IEEE Trans. Power Electron.*, vol. 22, no. 1, pp. 54–62, Jan. 2007.

[17] M. Reuter, T. Friedl, S. Tenbohlen, and V. Kohler, "Emulation of conducted emissions of an automotive inverter for filter development in HV network," in *Proc. IEEE Int. Symp. Electromagn. Compat.*, Denver, CO, USA, 2013, pp. 236–241.

[18] J. Su and L. Xing, "Parameterization of three-phase electric machine models for EMI simulation," *IEEE Trans. Power Electron.*, vol. 29, no. 1, pp. 36–41, Jan. 2014.

[19] B. Toure, J.-L. Schanen, L. Gerbaud, T. Meynard, J. Roudet, and R. Ruelland, "EMC modeling of drives for aircraft applications: Modeling process, EMI filter optimization, and technological choice," *IEEE Trans. Power Electron.*, vol. 28, no. 3, pp. 1145–1156, Mar. 2013.

[20] Y. Koyama, M. Tanaka, and H. Akagi, "Modeling and analysis for simulation of common-mode noises produced by an inverter-driven air conditioner," *IEEE Trans. Ind. Appl.*, vol. 47, no. 5, pp. 2166–2174, Sept./Oct. 2011.

Natalia Bondarenko received the B.S. degree in applied mathematics and computer science and the M.S. degree in electrical and electronics engineering both from Tbilisi State University, Tbilisi, Georgia, in 2006 and 2009, respectively. Since 2009, she has been working toward the Ph.D. degree in electrical engineering at the EMC Laboratory, Missouri University of Science and Technology, Rolla, MO, USA.

From 2005 to 2009, she was with EMCoS, Ltd., working on consulting projects for automotive electromagnetic compatibility (EMC). Her research interests include EMC of power inverter systems, system-level EMC/electromagnetic interference modeling and measurements methods.

Li Zhai received the B.S. degree in electrical engineering from the Shandong University of Science and Technology, Shandong, China, in 1996, the M.S. degree in mechanical and electronic engineering from the Shandong Agriculture University, Shandong, in 2001, and the Ph.D. degree in vehicle engineering from the Beijing Institute of Technology, Beijing, China, in 2004.

Since 2009, she has been an Associate Professor at the National Engineering Laboratory for Electric Vehicle, Beijing Institute of Technology. From 2013 to 2014, she was a Visitor Scholar with the EMC Laboratory, Missouri University of Science and Technology, Rolla, MO, USA. Her research interests include electromagnetic compatibility/electromagnetic interference of power electronics in electrical vehicles, and electrical machine control.

Bingjie Xu received the B.S. degree in electrical engineering from the Huazhong University of Science and Technology, Wuhan, China, in 2014.

In summer 2014, she was a Visiting Student at the EMC Laboratory, Missouri University of Science and Technology, Rolla, MO, USA. Her research interests include communication systems, EM simulations and signal integrity.

Guanghua Li received the B.S. and M.S. degrees in electrical engineering from Sichuan University, Sichuan, China, in 2008 and 2011, respectively. He is currently working toward the Ph.D. degree in electrical engineering at the EMC Laboratory, Missouri University of Science and Technology, Rolla, MO, USA.

His research interests include near-field probe development, radiated emission modeling technique, and crosstalk analysis.

Tamar Makharashvili received the B.S. degree (with highest honors) in electrical and electronics engineering from Tbilisi State University, Tbilisi, Georgia, in 2013, and is currently working toward the M.S. degree in electrical engineering at the EMC Laboratory, Missouri University of Science and Technology, Rolla, MO, USA.

From 2011 to 2013, she was with EMCoS, Ltd. Her research area includes numerical EM analysis, electromagnetic compatibility in power electronic systems.

David Loken received the B.S. degree in electrical engineering from North Dakota State University, Fargo, ND, USA, in 2006.

He is currently with John Deere Electronic Solutions, Fargo. His research interests include switching power converters, machine drives, machine control, and electromagnetic compatibility of power converters.

Phil Berger received the B.S. degree in electrical engineering from the University of Utah, Salt Lake City, UT, USA.

He is currently a Research Associate at the Missouri University of Science and Technology, Rolla, MO, USA.

Mr. Berger is a member of the IEEE EMC Society where he is the Chair of Technical Committee #4. He is also the Vice Chair of the Cedar Rapids Iowa section IEEE EMC Society. As a member of the Society of Automotive Engineers for 18 years, he participates in the EMC Standards Committee.

Thomas P. Van Doren (S'60–M'69–SM'96–F'01) received the B.S., M.S., and Ph.D. degrees from the University of Missouri-Rolla, Rolla, MO, USA, in 1962, 1963, and 1969, respectively.

From 1963 to 1965, he served as an Officer in the U.S. Army Security Agency. From 1965 to 1967, he was a Microwave Engineer with Collins Radio Company, Dallas, TX. Since 1967, he has been a member of the Electrical Engineering faculty at the University of Missouri-Rolla, where he is currently Professor Emeritus of electrical and computer engineering. He has conducted research and education in electromagnetic compatibility for the past 28 years. More than 18 000 engineers and technicians from 105 companies and government agencies have attended his "Grounding and Shielding" and "Circuit Board Layout" courses.

Daryl G. Beetner (S'89–M'98–SM'03) received the B.S. degree in electrical engineering from Southern Illinois University at Edwardsville, Edwardsville, IL, USA, in 1990, and the M.S. and D.Sc. degrees in electrical engineering from Washington University in St Louis, St. Louis, MO, USA, in 1994 and 1997, respectively.

He is a Professor and the Chair of electrical and computer engineering at the Missouri University of Science and Technology (formerly called the University of Missouri-Rolla), Rolla, MO. He conducts research with the EMC Laboratory at Missouri S&T on a wide variety of topics including electromagnetic compatibility at the chip and system level and detection and neutralization of explosive devices.

Dr. Beetner is an Associate Editor for the IEEE TRANSACTIONS ON INSTRUMENTATION AND MEASUREMENT.